

TABLE I. Variational ground state energy per site E_0 (in units of J) and the expectation of the flux operator $w_p = \langle \hat{W}_p \rangle$.

	<i>Exact</i>	<i>D</i> = 2 (loop-gas)	<i>D</i> = 4 (loop-gas)	<i>D</i> = 2 (optimized)	<i>D</i> = 3 (optimized)	<i>D</i> = 4 (optimized)	<i>D</i> = 5 (optimized)
E_0	-0.78730	-0.65399	-0.78576	-0.75624	-0.77194	-0.78695	-0.78714
w_p	1	1	1	0.02533	0.88148	0.999996	0.99933

bond dimension D . The PEPS virtual legs are along the nearest-neighbor x , y , and z bonds as depicted in Eq.(2). The Kitaev model is distinguished by the gauge symmetry characterized by flux operators $\hat{W}_p = \sigma_1^x \sigma_2^y \sigma_3^z \sigma_4^x \sigma_5^y \sigma_6^z$ linked to the p -th hexagon plaquette in Eq.(2). Due to $\hat{W}_p^2 = 1$, their eigenvalues are $w_p = \pm 1$ with \mathbb{Z}_2 gauge nature. For $w_p = +1$, the plaquette is vortex-free, while for $w_p = -1$, it possesses a vortex (vison). Under periodic boundary conditions, the product of all flux operators equals 1, i.e., $\prod_p \hat{W}_p = 1$. This topological constraint imposes limitations, allowing only excitations with an even vison number, indicating a \mathbb{Z}_2 gauge symmetry in the local tensor to encode the topological property [22].

The optimization of the ground state PEPS is accomplished through variational energy minimization techniques, employing gradient optimization methods [42, 43]. Here, we use the corner transfer matrix renormalization group (CTMRG) method [44–46] for tensor contractions with a truncation dimension $\chi = 64$. The energy gradient is obtained through reverse mode automatic differentiation [47]. In contrast to prior work [48], where optimization started from a symmetric initial PEPS, our unbiased approach initiates from a randomly generated state. Table. I lists the results of the ground-state variational energy and the flux operator expectation. Additionally, results from the loop-gas PEPS wave function, featuring a meticulously designed gauge structure [27], are included for comparison. For a small bond dimension $D = 2$, the optimized PEPS exhibits a lower variational energy than the loop-gas PEPS. However, this comes at the cost of losing gauge symmetry, as evidenced by the flux expectation w_p being close to zero, deviating from the exact result $w_p = 1$. With increasing bond dimension D , the variational energy is further optimized as anticipated, and concurrently, we observe the flux expectation w_p approaching the exact result $w_p = 1$ for $D = 4$, thereby displaying the essential vortex-free nature of the Kitaev spin liquid ground state. Further improvement for the energy can be achieved with $D = 5$, while the flux expectation remains essentially unchanged.

Gauge symmetry in excited state PEPS– From the ground state, local excited state PEPSs are constructed as $|B_i\rangle = \sum_{abca'b'; s_{\alpha_i}, s_{\beta_i}} B_{aba'b'}^{s_{\alpha_i}, s_{\beta_i}} \frac{\partial}{\partial (A_{abc}^{s_{\alpha_i}} A_{a'b'c}^{s_{\beta_i}})} |\Psi(A)\rangle$ as

illustrated in the graph

$$|B_i\rangle = \cdots \begin{array}{c} \vdots \\ \text{---} w_4 \text{---} \text{---} w_2 \text{---} \text{---} w_1 \text{---} \cdots \\ \text{---} w_3 \text{---} \\ \vdots \end{array} \quad (3)$$

where the impurity tensor B acts on the two sites α_i and β_i within the i -th unit cell.

Once the ground state is the vortex-free state $|\psi(A); w_p = 1\rangle$, the excited state in Eq. (3) can be characterized by the eigenvalues $w_{1,2,3,4}$ of the four plaquette operators $\hat{W}_{1,2,3,4}$, denoted as $|B_i; \{w_{1,2,3,4}\}\rangle$. Other plaquettes are not perturbed, and thus $w_p = 1$ for $p \notin \{1, 2, 3, 4\}$. The eigen-equations $\hat{W}_p |B_i\rangle = w_p N_B |B_i\rangle$ for $p = 1, 2, 3, 4$, where N_B is the norm matrix of $|B_i\rangle$, can be diagonalized simultaneously as the flux operators commute with each other[49]. For the infinite PEPS simulation, the lattice has the effective open boundary condition and thus odd-vison excitations are also allowed. $w_{1,2,3,4}$ take the value of ± 1 , independent of each other, and $|B_i; \{w_{1,2,3,4}\}\rangle$ has $2^4 = 16$ different vison configurations. Fig. 1(a) illustrates the absolute value distributions of $w_{1,2,3,4}$ for the optimized PEPS with $D = 4$, in which all values closely approximate the exact value of 1 within a numerical error of less than 2.5%, affirming the

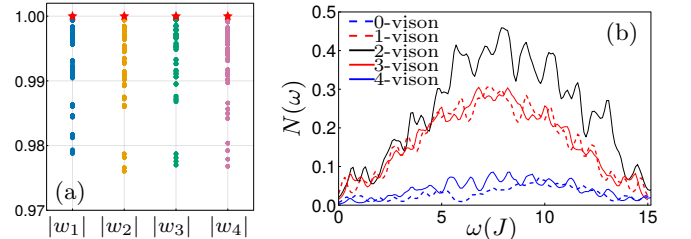


FIG. 1. (a) Absolute value distributions of $w_{1,2,3,4}$, with red stars denoting the results for the ground state PEPS with $D = 4$. (b) Zero momentum low-energy DOS with a broadening $\sigma = 0.2J$ for the 0, 1, 2, 3, and 4-vison sectors. The full DOS is expected to be captured up to an energy of order 5-7 roughly, above which other excitations not included here are expected to contribute.

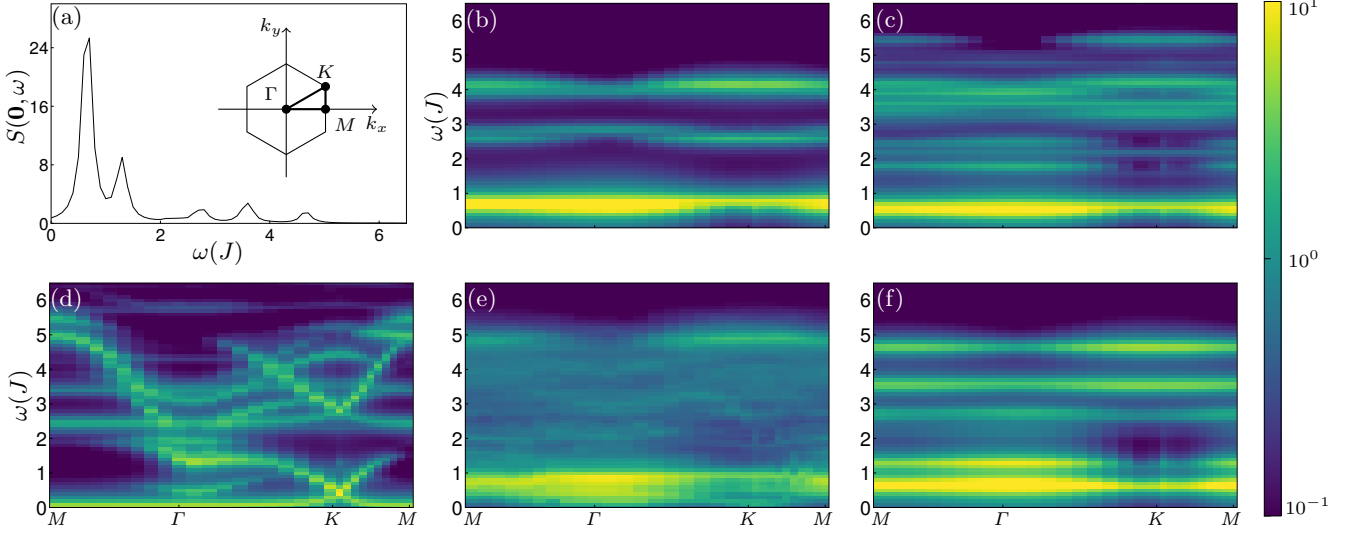


FIG. 2. Computed spin dynamics with a Lorentzian broadening $\sigma = 0.1J$. (a) Zero momentum dynamics for optimized PEPS with $D = 4$. The first Brillouin zone and the momentum path for the spectral function are shown in the inset. Momentum-resolved spin dynamics for loop-gas PEPS with $D = 2$ in (b) and $D = 4$ in (c), optimized PEPS with $D = 2$ in (d), $D = 3$ in (e), and $D = 4$ in (f).

gauge symmetry in both ground and excited PEPSs.

By taking a linear superposition of all locally perturbed states, we can construct translational-invariant excited states $|\mathfrak{B}_{\mathbf{q}}\rangle = \sum_i e^{i\mathbf{q}\cdot\mathbf{r}_i} |B_i\rangle$ with momentum \mathbf{q} . Spanned by these excited states (hereafter labeled by m), the effective Hamiltonian is given by

$$\mathcal{H}_{\mathbf{q}}|\mathfrak{B}_{\mathbf{q}}^m\rangle = \lambda_{\mathbf{q}}^m N_{\mathfrak{B}_{\mathbf{q}}}|\mathfrak{B}_{\mathbf{q}}^m\rangle, \quad (4)$$

where $\mathcal{H}_{\mathbf{q}}$ and $N_{\mathfrak{B}_{\mathbf{q}}}$ represent the effective Hamiltonian and norm matrices.

The locally conserved vison makes the Hamiltonian (4) block-diagonal. For better clarity, we categorize the 16 vison configurations into distinct vison sectors, spanning 0 to 4 visons. Each sector corresponds to a specific number of vison configurations: 1 for 0-vison, 4 for 1-vison, 6 for 2-vison, 4 for 3-vison, and 1 for 4-vison. The total DOS (at momentum $\mathbf{q} = \mathbf{0}$) shown in Fig.1(b) within each sector reveals fractionalized continua, indicative of multiple-spinon excitations.

Spin dynamics – Spin excited states $\sigma_s^\gamma|\psi(A)\rangle$ on the s -site can be also labeled by the surrounding vison configurations $w_{1,2,3,4}$ since the flux operator \hat{W}_p commutes or anti-commutes with local operators. Examining the plaquettes in Eq.(2), when σ^x is applied on the site 2, 3, 5, or 6, we have $\sigma_s^x \hat{W}_p \sigma_s^x = -\hat{W}_p$; when σ^x acts on the site 1 or 4, we have $\sigma_s^x \hat{W}_p \sigma_s^x = \hat{W}_p$. Consequently, the spin excited state $\sigma_s^x|\psi(A)\rangle$ introduces a vison in each of the two plaquettes containing the bond along the x -direction, adjacent to the s -site [8, 9]. Similar outcomes apply for

$\sigma_s^y|\psi(A)\rangle$ and $\sigma_s^z|\psi(A)\rangle$, leading to the following

$$(w_1, w_2, w_3, w_4) = \begin{cases} (+1, -1, -1, +1), & \sigma_{\alpha_i}^x |\psi(A)\rangle \\ (+1, -1, -1, +1), & \sigma_{\beta_i}^x |\psi(A)\rangle \\ (+1, -1, +1, -1), & \sigma_{\alpha_i}^y |\psi(A)\rangle \\ (-1, +1, -1, +1), & \sigma_{\beta_i}^y |\psi(A)\rangle \\ (+1, +1, -1, -1), & \sigma_{\alpha_i}^z |\psi(A)\rangle \\ (-1, -1, +1, +1), & \sigma_{\beta_i}^z |\psi(A)\rangle \end{cases} \cdot (5)$$

The dynamical spin correlation function is defined as

$$S_{ij}^{\gamma\gamma}(t) = \langle \psi(A) | \sigma_j^\gamma(t) \sigma_i^\gamma | \psi(A) \rangle, \quad (6)$$

from which we obtain the spin dynamics

$$S(\mathbf{q}, \omega) = \sum_{m\gamma} |\langle \mathfrak{B}_{\mathbf{q}}^m | S_{\mathbf{q}}^\gamma \rangle|^2 \delta(\omega - (\lambda_{\mathbf{q}}^m - \lambda_0)). \quad (7)$$

Figure 2 presents the numerical results on the spin dynamics $S(\mathbf{q}, \omega)$ for different ground state PEPSs. Fig. 2(a) displays $S(0, \omega)$ for the optimized PEPS with $D = 4$ in which the peak around $\omega = 0.5J$ corresponds to the 2-vison-related excitations.

The spin excited states belong to the 2-vison sector. Vison excitations, static and conserved over time, adhere to the gauge symmetry, leading to an ultra-short spin correlation with a strict vanishing of correlations beyond nearest neighbors [8, 9]. This ultra-short correlation manifests in flat momentum-resolved spin dynamics, providing a crucial validation for our numerical findings. Faithfully capturing the gauge structure in both the ground-state and excited PEPS, as exemplified by the analytical loop-gas wave function in Fig. 2 (b) and

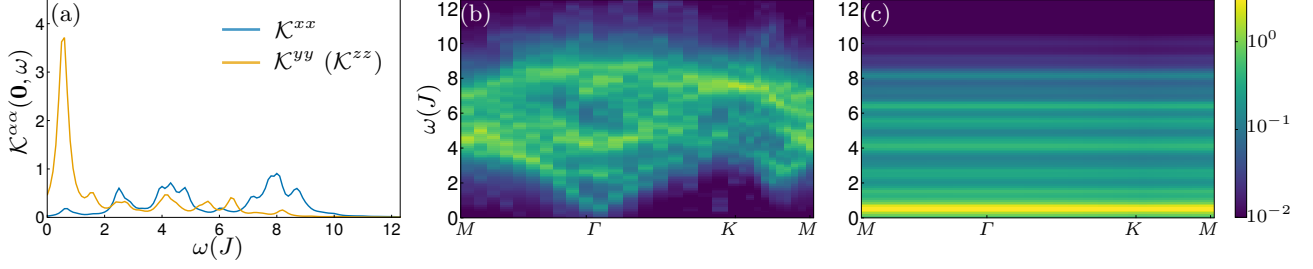


FIG. 3. Computed spin dimer dynamics with a Lorentzian broadening $\sigma = 0.2J$ for an optimized PEPS with $D = 4$; (a) $\mathcal{K}^{xx}(\mathbf{0}, \omega)$ and $\mathcal{K}^{yy}(\mathbf{0}, \omega)$ ($\mathcal{K}^{zz}(\mathbf{0}, \omega)$); (b) color plot of $\mathcal{K}^{xx}(\mathbf{q}, \omega)$; (c) color plot of $\mathcal{K}^{yy}(\mathbf{q}, \omega)$ ($\mathcal{K}^{zz}(\mathbf{q}, \omega)$).

(c) and the optimized wave function with $D = 4$ in Fig. 2(f), the observed flat pattern in spin dynamics signifies an exceptionally weak dependence on momentum. In contrast, the gauge structure is entirely lost in the optimized wave function with $D = 2$, resulting in dispersive spin dynamics in Fig. 2 (d). It is noteworthy that despite the loop-gas wave function with $D = 2$ providing a less accurate variational ground state, it accurately captures the gauge structure, ensuring a correct representation of short spin correlation physics in Fig. 2 (b) [49].

Spin-dimer dynamics – From Eq.(5), we can easily prove the following for the dimer excited states

$$(w_1, w_2, w_3, w_4) = \begin{cases} (+1, +1, +1, +1), \mathcal{K}_i^x |\psi(A)\rangle \\ (-1, -1, -1, -1), \mathcal{K}_i^y |\psi(A)\rangle \\ (-1, -1, -1, -1), \mathcal{K}_i^z |\psi(A)\rangle \end{cases}, \quad (8)$$

with $\mathcal{K}_i^\gamma = \sigma_{\alpha_i}^\gamma \sigma_{\beta_i}^\gamma$ and i refers to an x-bond. Therefore, $\mathcal{K}_i^x |\psi(A)\rangle$ belongs to the 0-vison sector, whereas $\mathcal{K}_i^y |\psi(A)\rangle$ and $\mathcal{K}_i^z |\psi(A)\rangle$ reside in the 4-vison sector [10]. These distinct vison sectors result in markedly different spin-dimer correlations which are defined as

$$\mathcal{K}_{ij}^{\gamma\gamma}(t) = \langle \psi(A) | \mathcal{K}_j^\gamma(t) \mathcal{K}_i^\gamma | \psi(A) \rangle, \quad (9)$$

from which we have the spin-dimer dynamical structural factor

$$\mathcal{K}^{\gamma\gamma}(\mathbf{q}, \omega) = \sum_m |\langle \mathfrak{B}_q^m | \mathcal{K}_q^\gamma | \rangle|^2 \delta(\omega - (\lambda_q^m - \lambda_0)). \quad (10)$$

Figure 3 presents the spin-dimer dynamics for the optimized PEPS with $D = 4$. The zero-momentum spin-dimer dynamics $\mathcal{K}(\mathbf{0}, \omega)$, which is potentially probed in the Raman scattering measurements [13–17], displays a 4-vison peak around $0.5J$ in \mathcal{K}^{yy} and \mathcal{K}^{zz} , as shown in Fig. 3(a). The momentum-dependent spin-dimer dynamics, potentially measurable in RIXS experiments [18, 19], are depicted in Fig. 3(b)-(c). Remarkably, the spin-dimer dynamics $\mathcal{K}^{xx}(\mathbf{q}, \omega)$ depicted in Fig. 3(b) displays a dispersive fractional continuum in the zero-vison sector spanning the entire Brillouin zone. This characteristic feature is in agreement with the model Eq. (1) being gapless [4], and provides a distinctive signature of spinon-pair

excitations, particularly relevant for interpreting RIXS measurements. In contrast, the selection rule imposed by vison conservation – all excitations created by \mathcal{K}_i^y and \mathcal{K}_i^z belong to the 4-vison sector – results in a flat momentum-resolved dynamics ($\mathcal{K}^{yy}(\mathbf{q}, \omega)$ and $\mathcal{K}^{zz}(\mathbf{q}, \omega)$), as seen in Fig. 3(c)[50]. The distinctive momentum dependences of the spin-dimer dynamics highlight the primordial role of the gauge structure in the optimized PEPS with $D = 4$.

Conclusion – In conclusion, our investigation has delved into the intricate gauge structure of projected entangled pair state (PEPS) simulations, extending our scrutiny beyond the ground state to low-lying excited states within the Kitaev honeycomb model. Importantly, we have demonstrated that gauge symmetry is not maintained solely in the unbiased optimized ground state achieved through variational optimization; rather, it seamlessly extends to excited states constructed by the PEPS adaptive local mode approximation method.

Furthermore, our simulations of low-energy dynamics in spin and spin-dimer correlations establish connections with experimental observations such as INS and light scattering (Raman and RIXS) experiments. The selection rule imposed by locally conserved vison flux yields flat momentum-resolved dynamics if the excited states contain vison excitations. This study underscores the efficacy of employing PEPS to explore gauge symmetry and fractionalized excitations within topologically ordered states, presenting a robust framework for further investigations in the realm of quantum many-body systems.

Acknowledgment – This work is supported by the National Key Research and Development Program of China (Grant No. 2021YFA1400400), Shenzhen Fundamental Research Program (Grant No. JCYJ20220818100405013), the Guangdong Innovative and Entrepreneurial Research Team Program (Grants No. 2017ZT07C062), Shenzhen Key Laboratory of Advanced Quantum Functional Materials and Devices (Grant No. ZDSYS20190902092905285), Guangdong Basic and Applied Basic Research Foundation (Grant No. 2020B1515120100). J.-Y.C. was supported by Open Research Fund Program of the State Key Lab-

oratory of Low-Dimensional Quantum Physics (project No. KF202207), Fundamental Research Funds for the Central Universities, Sun Yat-sen University (project No. 23qnp60), a startup fund from Sun Yat-sen University, the Innovation Program for Quantum Science and Technology 2021ZD0302100, and National Natural Science Foundation of China (NSFC) (grant No. 12304186). Part of the calculations reported were performed on resources provided by the Guangdong Provincial Key Laboratory of Magnetoelectric Physics and Devices, No. 2022B1212010008. This work was also supported by the TNTOP ANR-18-CE30-0026-01 grant awarded by the French Research Council.

* chenjiy3@mail.sysu.edu.cn

† didier.poilblanc@irsamc.ups-tlse.fr

‡ meijw@sustech.edu.cn

- [1] A. Kitaev and J. Preskill, Topological entanglement entropy, *Phys. Rev. Lett.* **96**, 110404 (2006).
- [2] M. Levin and C. P. Nave, Tensor renormalization group approach to two-dimensional classical lattice models, *Phys. Rev. Lett.* **99**, 120601 (2007).
- [3] X.-G. Wen, Choreographed entanglement dances: Topological states of quantum matter, *Science* **363**, eaal3099 (2019).
- [4] A. Kitaev, Anyons in an exactly solved model and beyond, *Annals of Physics* **321**, 2 (2006).
- [5] G. Jackeli and G. Khaliullin, Mott Insulators in the Strong Spin-Orbit Coupling Limit: From Heisenberg to a Quantum Compass and Kitaev Models, *Phys. Rev. Lett.* **102**, 017205 (2009).
- [6] J. c. v. Chaloupka, G. Jackeli, and G. Khaliullin, Kitaev-Heisenberg Model on a Honeycomb Lattice: Possible Exotic Phases in Iridium Oxides $A_2\text{IrO}_3$, *Phys. Rev. Lett.* **105**, 027204 (2010).
- [7] H. Takagi, T. Takayama, G. Jackeli, G. Khaliullin, and S. E. Nagler, Concept and realization of kitaev quantum spin liquids, *Nature Reviews Physics* **1**, 264 (2019).
- [8] G. Baskaran, S. Mandal, and R. Shankar, Exact Results for Spin Dynamics and Fractionalization in the Kitaev Model, *Phys. Rev. Lett.* **98**, 247201 (2007).
- [9] J. Knolle, D. L. Kovrizhin, J. T. Chalker, and R. Moessner, Dynamics of a Two-Dimensional Quantum Spin Liquid: Signatures of Emergent Majorana Fermions and Fluxes, *Phys. Rev. Lett.* **112**, 207203 (2014).
- [10] J. Knolle, G.-W. Chern, D. L. Kovrizhin, R. Moessner, and N. B. Perkins, Raman Scattering Signatures of Kitaev Spin Liquids in $A_2\text{IrO}_3$ Iridates with $A = \text{Na}$ or Li , *Phys. Rev. Lett.* **113**, 187201 (2014).
- [11] A. Banerjee, C. A. Bridges, J.-Q. Yan, A. A. Aczel, L. Li, M. B. Stone, G. E. Granroth, M. D. Lumsden, Y. Yiu, J. Knolle, S. Bhattacharjee, D. L. Kovrizhin, R. Moessner, D. A. Tennant, D. G. Mandrus, and S. E. Nagler, Proximate Kitaev quantum spin liquid behaviour in a honeycomb magnet, *Nature Materials* **15**, 733 (2016).
- [12] A. Banerjee, J. Yan, J. Knolle, C. A. Bridges, M. B. Stone, M. D. Lumsden, D. G. Mandrus, D. A. Tennant, R. Moessner, and S. E. Nagler, Neutron scattering in the proximate quantum spin liquid $\alpha - \text{RuCl}_3$, *Science* **356**, 1055 (2017).
- [13] L. J. Sandilands, Y. Tian, K. W. Plumb, Y.-J. Kim, and K. S. Burch, Scattering Continuum and Possible Fractionalized Excitations in $\alpha\text{-RuCl}_3$, *Phys. Rev. Lett.* **114**, 147201 (2015).
- [14] J. Nasu, J. Knolle, D. L. Kovrizhin, Y. Motome, and R. Moessner, Fermionic response from fractionalization in an insulating two-dimensional magnet, *Nature Physics* **12**, 912 (2016).
- [15] A. Glamazda, P. Lemmens, S. H. Do, Y. S. Choi, and K. Y. Choi, Raman spectroscopic signature of fractionalized excitations in the harmonic-honeycomb iridates β - and γ - Li_2IrO_3 , *Nature Communications* **7**, 12286 (2016).
- [16] G. Li, X. Chen, Y. Gan, F. Li, M. Yan, F. Ye, S. Pei, Y. Zhang, L. Wang, H. Su, J. Dai, Y. Chen, Y. Shi, X. Wang, L. Zhang, S. Wang, D. Yu, F. Ye, J.-W. Mei, and M. Huang, Raman spectroscopy evidence for dimerization and Mott collapse in $\alpha\text{-RuCl}_3$ under pressures, *Phys. Rev. Materials* **3**, 023601 (2019).
- [17] S. Pei, L.-L. Huang, G. Li, X. Chen, B. Xi, X. Wang, Y. Shi, D. Yu, C. Liu, L. Wang, F. Ye, M. Huang, and J.-W. Mei, Magnetic Raman continuum in single-crystalline $\text{H}_3\text{LiIr}_2\text{O}_6$, *Phys. Rev. B* **101**, 201101 (2020).
- [18] J. Kim, J. c. v. Chaloupka, Y. Singh, J. W. Kim, B. J. Kim, D. Casa, A. Said, X. Huang, and T. Gog, Dynamic spin correlations in the honeycomb lattice Na_2IrO_3 measured by resonant inelastic x-ray scattering, *Phys. Rev. X* **10**, 021034 (2020).
- [19] A. de la Torre, B. Zager, F. Bahrami, M. H. Upton, J. Kim, G. Fabbri, G.-H. Lee, W. Yang, D. Haskel, F. Tafti, and K. W. Plumb, Momentum-independent magnetic excitation continuum in the honeycomb iridate $\text{h}_3\text{liir}_2\text{o}_6$, *Nature Communications* **14**, 5018 (2023).
- [20] F. Verstraete and J. I. Cirac, Renormalization algorithms for quantum-many body systems in two and higher dimensions, *arXiv preprint* (2004), cond-mat/0407066.
- [21] J. I. Cirac, D. Pérez-García, N. Schuch, and F. Verstraete, Matrix product states and projected entangled pair states: Concepts, symmetries, theorems, *Rev. Mod. Phys.* **93**, 045003 (2021).
- [22] N. Schuch, I. Cirac, and D. Pérez-García, PEPS as ground states: Degeneracy and topology, *Annals of Physics* **325**, 2153 (2010).
- [23] X. Chen, B. Zeng, Z.-C. Gu, I. L. Chuang, and X.-G. Wen, Tensor product representation of a topological ordered phase: Necessary symmetry conditions, *Phys. Rev. B* **82**, 165119 (2010).
- [24] N. Schuch, D. Poilblanc, J. I. Cirac, and D. Pérez-García, Resonating valence bond states in the PEPS formalism, *Phys. Rev. B* **86**, 115108 (2012).
- [25] S. Jiang and Y. Ran, Symmetric tensor networks and practical simulation algorithms to sharply identify classes of quantum phases distinguishable by short-range physics, *Phys. Rev. B* **92**, 104414 (2015).
- [26] J.-W. Mei, J.-Y. Chen, H. He, and X.-G. Wen, Gapped spin liquid with \mathbb{Z}_2 topological order for the kagome heisenberg model, *Phys. Rev. B* **95**, 235107 (2017).
- [27] H.-Y. Lee, R. Kaneko, T. Okubo, and N. Kawashima, Gapless Kitaev spin liquid to classical string gas through tensor networks, *Phys. Rev. Lett.* **123**, 087203 (2019).
- [28] J.-Y. Chen, S. Capponi, A. Wietek, M. Mambrini, N. Schuch, and D. Poilblanc, $\text{SU}(3)_1$ chiral spin liquid on the square lattice: A view from symmetric projected entangled pair states, *Phys. Rev. Lett.* **125**, 017201 (2020).

- [29] A. Francuz and J. Dziarmaga, Determining non-abelian topological order from infinite projected entangled pair states, *Phys. Rev. B* **102**, 235112 (2020).
- [30] N. Schuch, D. Poilblanc, J. I. Cirac, and D. Pérez-García, Topological order in the projected entangled-pair states formalism: Transfer operator and boundary hamiltonians, *Phys. Rev. Lett.* **111**, 090501 (2013).
- [31] H. He, H. Moradi, and X.-G. Wen, Modular matrices as topological order parameter by a gauge-symmetry-preserved tensor renormalization approach, *Phys. Rev. B* **90**, 205114 (2014).
- [32] S. P. G. Crone and P. Corboz, Detecting a Z_2 topologically ordered phase from unbiased infinite projected entangled-pair state simulations, *Phys. Rev. B* **101**, 115143 (2020).
- [33] L. Vanderstraeten, M. Mariën, F. Verstraete, and J. Haegeman, Excitations and the tangent space of projected entangled-pair states, *Phys. Rev. B* **92**, 201111 (2015).
- [34] L. Vanderstraeten, J. Haegeman, and F. Verstraete, Simulating excitation spectra with projected entangled-pair states, *Phys. Rev. B* **99**, 165121 (2019).
- [35] B. Ponsioen and P. Corboz, Excitations with projected entangled pair states using the corner transfer matrix method, *Phys. Rev. B* **101**, 195109 (2020).
- [36] B. Ponsioen, F. F. Assaad, and P. Corboz, Automatic differentiation applied to excitations with projected entangled pair states, *SciPost Phys.* **12**, 006 (2022).
- [37] B. Ponsioen, J. Hasik, and P. Corboz, Improved summations of N-point correlation functions of projected entangled-pair states, *arXiv preprint* (2023), 2306.13327.
- [38] W.-L. Tu, L. Vanderstraeten, N. Schuch, H.-Y. Lee, N. Kawashima, and J.-Y. Chen, Generating function for projected entangled-pair states (2023), *arXiv:2307.08083 [cond-mat.str-el]*.
- [39] R. P. Feynman, Atomic theory of the λ transition in helium, *Phys. Rev.* **91**, 1291 (1953).
- [40] R. Chi, Y. Liu, Y. Wan, H.-J. Liao, and T. Xiang, Spin excitation spectra of anisotropic spin-1/2 triangular lattice Heisenberg antiferromagnets, *Phys. Rev. Lett.* **129**, 227201 (2022).
- [41] J. Hasik, M. Van Damme, D. Poilblanc, and L. Vanderstraeten, Simulating Chiral Spin Liquids with Projected Entangled-Pair States, *Phys. Rev. Lett.* **129**, 177201 (2022).
- [42] L. Vanderstraeten, J. Haegeman, P. Corboz, and F. Verstraete, Gradient methods for variational optimization of projected entangled-pair states, *Phys. Rev. B* **94**, 155123 (2016).
- [43] P. Corboz, Variational optimization with infinite projected entangled-pair states, *Phys. Rev. B* **94**, 035133 (2016).
- [44] T. Nishino and K. Okunishi, Corner transfer matrix renormalization group method, *J. Phys. Soc. Jpn.* **65**, 891 (1996).
- [45] R. Orús and G. Vidal, Simulation of two-dimensional quantum systems on an infinite lattice revisited: Corner transfer matrix for tensor contraction, *Phys. Rev. B* **80**, 094403 (2009).
- [46] P. Corboz, T. M. Rice, and M. Troyer, Competing states in the t - J model: Uniform d -wave state versus stripe state, *Phys. Rev. Lett.* **113**, 046402 (2014).
- [47] H.-J. Liao, J.-G. Liu, L. Wang, and T. Xiang, Differentiable programming tensor networks, *Phys. Rev. X* **9**, 031041 (2019).
- [48] I. V. Lukin and A. G. Sotnikov, Variational optimization of tensor-network states with the honeycomb-lattice corner transfer matrix, *Phys. Rev. B* **107**, 054424 (2023).
- [49] Supplementary Materials for CTMRG methods of the $w_{1,2,3,4}$ evaluation and the gauge structure of excited state based on the loop-gas PEPS.
- [50] For Raman and RIXS experiments, $\mathcal{K}^{xx}(\mathbf{q}, \omega)$, $\mathcal{K}^{yy}(\mathbf{q}, \omega)$ and $\mathcal{K}^{zz}(\mathbf{q}, \omega)$ are simultaneously detected and not easily disentangled. Thus we expect the experimental spectra to reveal the flat dispersions embedded in the fractionalized continuum.

Supplementary material for “Gauge symmetry of excited states in projected entangled-pair state simulations”

COMPUTATING EXPECTATION OF THE FLUX OPERATOR

In our simulation, the honeycomb lattice is transformed into a square lattice through the combination of the A-B sublattices. The ground state is effectively described using an infinite projected entangled-pair state (iPEPS)

$$|\Psi(A)\rangle = \text{[Diagram: A honeycomb lattice on the left with blue and red arrows on its edges, followed by an arrow pointing to a square lattice on the right with blue arrows on its edges]} \quad (\text{S-1})$$

To detect the gauge symmetry, we apply the plaquette operator W_p directly to the states and compute the expectation, as illustrated in Fig. S1. We have verified that w_p of the ground state is close to 1, with precision up to 10^{-6} , under different boundary conditions. After obtaining the ground state, we proceed to construct the excited state using the local mode approximation, as illustrated in the main text. The expanded subspace of the impurity tensor has a dimension of $D^4d - 1$ (excluding the ground state). For numerical classification of the subspace according to flux number, we perform simultaneous diagonalization of W_1 , W_2 , W_3 , and W_4 using the eigen-equation:

$$\hat{W}_i |E\rangle = w_i N |E\rangle \quad i = 1, 2, 3, 4. \quad (\text{S-2})$$

Note that a small violation of the gauge symmetry in the optimized PEPS could yield a small deviation of exact commutativity of the \hat{W}_p and of the projectivity $\hat{W}_p^2 = 1$, and hence the values of $w_{1,2,3,4}$ may have small deviations from the exact value $w_p = \pm 1$, as shown in the main text. For convenience, we can compute the w_i of excited state by placing the impurity tensor on the four adjacent positions, respectively, as the Fig. S1(a). Notably, the odd vison only exists in open boundary conditions and has an exactly zero norm in periodic boundary conditions. Afterward, the subspace is classified into 16 sectors, and we can then diagonalize the Hamiltonian in each sector.

GAUGE STRUCTURE OF EXCITED STATES FOR THE LOOP-GAS PEPS

In this section, we interpret our result in terms of the analytical loop-gas PEPS for the Kitaev spin liquid [27], in which the gauge symmetry is explicitly incorporated.

In an effort to preserve the symmetries of the Kitaev spin liquid ground state, a straightforward naive trial wave function for the Kitaev model is the GHZ state along the (111)-direction

$$|\text{GHZ}\rangle = \bigotimes_i |(111)\rangle_i + \bigotimes_i |(-1 - 1 - 1)\rangle_i. \quad (\text{S-3})$$

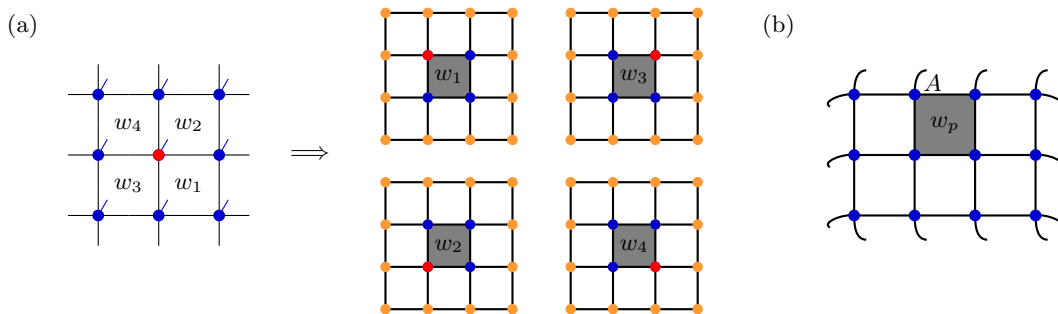


FIG. S1. Computing the flux number under different boundary conditions. (a) CTMRG with the open boundary condition. The calculation of different w_p values is achieved by placing impurity tensor on different sites. (b) Exact contraction on the 3×4 torus.

When we rotate the (111)-direction into the \tilde{z} -axis in the rotated axis, where the spin indices are rotated as $|\tilde{s}\rangle = \mathcal{S}|s\rangle$ with $\mathcal{S} = \exp(-i\frac{\pi}{8}\sigma^z)\exp(-i\frac{\theta}{2}\sigma^y)$ ($\cos\theta = \frac{1}{\sqrt{3}}$), it becomes straightforward to write down the non-zero elements of the local tensor for the GHZ state $T_{111}^{\tilde{s}=\uparrow} = T_{222}^{\tilde{s}=\downarrow}(2,2,2) = 1$. We obtain the local tensor for the (111)-GHZ as $T_{abc}^s = \sum_{\tilde{s}} \mathcal{S}_{s\tilde{s}} T_{abc}^{\tilde{s}}$ by applying the spin-rotation operator \mathcal{S} .

The (111)-GHZ state not only exhibits inadequate variational energy but also lacks the crucial property of being an eigenstate of the vortex operator W_p , a characteristic essential for maintaining the vortex-free nature of the Kitaev spin-liquid ground state. To address the vortex-related challenge, Lee et al. introduced the loop gas operator \hat{Q}_{LG} layer atop the GHZ state with the local tensor

$$\begin{array}{cc} \begin{array}{c} 1 \\ | \\ 1 \end{array} \begin{array}{c} \diagup \\ | \\ \diagdown \end{array} \begin{array}{c} 1 \\ | \\ 1 \end{array} = \mathbf{1}_2 & \begin{array}{c} 2 \\ | \\ 2 \end{array} \begin{array}{c} \diagup \\ | \\ \diagdown \end{array} \begin{array}{c} 1 \\ | \\ 1 \end{array} = \sigma^x \\ \begin{array}{c} 1 \\ | \\ 2 \end{array} \begin{array}{c} \diagup \\ | \\ \diagdown \end{array} \begin{array}{c} 2 \\ | \\ 2 \end{array} = \sigma^y & \begin{array}{c} 2 \\ | \\ 2 \end{array} \begin{array}{c} \diagup \\ | \\ \diagdown \end{array} \begin{array}{c} 1 \\ | \\ 1 \end{array} = \sigma^z \end{array}, \quad (\text{S-4})$$

which preserves the symmetries of the Kitaev model, and additionally possesses the \mathbb{Z}_2 gauge structure

$$\begin{array}{c} \diagup \\ | \\ \diagdown \end{array} = \begin{array}{c} \sigma^z \\ \diagup \\ | \\ \diagdown \end{array} \sigma^z, \quad (\text{S-5})$$

$$\begin{array}{c} \diagup \\ | \\ \diagdown \end{array} = \begin{array}{c} \tilde{\sigma}^y \\ \diagup \\ | \\ \diagdown \end{array} \begin{array}{c} \sigma^x \\ \diagup \\ | \\ \diagdown \end{array} \begin{array}{c} \sigma^y \\ \diagup \\ | \\ \diagdown \end{array} = \begin{array}{c} \sigma^y \\ \diagup \\ | \\ \diagdown \end{array} \begin{array}{c} \tilde{\sigma}^y \\ \diagup \\ | \\ \diagdown \end{array} = \begin{array}{c} \tilde{\sigma}^y \\ \diagup \\ | \\ \diagdown \end{array} \begin{array}{c} \sigma^z \\ \diagup \\ | \\ \diagdown \end{array} \tilde{\sigma}^y, \quad (\text{S-6})$$

with $\tilde{\sigma}^y = (\sigma^x - \sigma^y)/\sqrt{2}$ and satisfying the following eigen equations

$$\begin{array}{ccc} \begin{array}{c} \diagup \\ | \\ \diagdown \end{array} & = & \begin{array}{c} \tilde{\sigma}^y \\ \diagup \\ | \\ \diagdown \end{array} \\ \begin{array}{c} \diagup \\ | \\ \diagdown \end{array} & = & \begin{array}{c} \sigma^z \\ \diagup \\ | \\ \diagdown \end{array} \end{array}, \quad (\text{S-7})$$

where $\begin{array}{c} \diagup \\ | \\ \diagdown \end{array}$ denotes the vortex operator W_p . The loop gas operator \hat{Q}_{LG} enriches the gauge symmetry of the GHZ state. When applied to the GHZ state, it yields the gauged GHZ state as the loop-gas PEPS

$$|\text{GHZ}\rangle_{\text{g}} = \hat{Q}_{\text{LG}}|\text{GHZ}\rangle, \quad (\text{S-8})$$

with the local tensor $\begin{array}{c} b_2 \\ \diagup \\ b_1 \end{array} \begin{array}{c} \diagup \\ | \\ \diagdown \end{array} \begin{array}{c} a_2 \\ \diagup \\ a_1 \end{array}$, which can be readily demonstrated to manifest a vortex-free character according to the eigen equations in Eq.(S-7).

Numerically verifying the ground state of the loop-gas PEPS, we confirm its vortex-free nature with $w_p = 1$. Additionally, we examine the excited states with local impurity tensors, finding that they exhibit $w_p = \pm 1$ for $p = 1, 2, 3, 4$. Specifically, for the $D = 2$ loop-gas PEPS, where the GHZ state is replaced by the product state $\bigotimes_i |(111)\rangle_i$, our numerical check involves both CTMRG contraction on an infinite lattice and exact contraction on a small 3×4 unit cluster. In the case of the torus-shaped cluster with periodic boundary conditions, excited states in the odd (1 and 3) vison sectors display zero norm. Conversely, for the cluster with open boundary conditions, excited states in the odd (1 and 3) vison sectors exhibit non-zero norm.

The local impurity tensors for the spin-excited states

$$\begin{aligned}
 |S_i^x\rangle &= \text{diag}_1(\sigma^x) = \text{diag}_2(\sigma^x) = \text{diag}_3(\sigma^z), \\
 |S_i^y\rangle &= \text{diag}_1(\sigma^y) = \text{diag}_2(\sigma^y) = \sigma^z \text{diag}_3, \\
 |S_i^z\rangle &= \text{diag}_1(\sigma^z) = \text{diag}_2(\sigma^z) = \sigma^z \text{diag}_3,
 \end{aligned} \tag{S-9}$$

and those for the spin-dimer excited states

$$\begin{aligned}
 |\mathcal{K}_i^x\rangle &= \text{diag}_1(\sigma^x \sigma^x) = \text{diag}_2(\sigma^x \sigma^x) = \text{diag}_3, \\
 |\mathcal{K}_i^y\rangle &= \text{diag}_1(\sigma^y \sigma^y) = \text{diag}_2(\sigma^y \sigma^y) = \sigma^z \text{diag}_3 \sigma^z, \\
 |\mathcal{K}_i^z\rangle &= \text{diag}_1(\sigma^z \sigma^z) = \text{diag}_2(\sigma^z \sigma^z) = \sigma_z \text{diag}_3.
 \end{aligned} \tag{S-10}$$

From the eigen equations in Eq.(S-7) for the loop operator, we notice that each σ_z on the virtual bond of \hat{Q}_{LG} (the blue layer in Eqs.(S-9) and (S-10)) introduces two-visons excitations associated with the bond. Thus we are ready to prove that the spin and spin-dimer excited states are the eigen-states of the vortex operator

$$W_p |E_i\rangle = \begin{cases} +|E_i\rangle, & p \notin i \\ -|E_i\rangle, & p \in i \end{cases}, \tag{S-11}$$

where $p \in i$ represents the vison excitation for the vortex operator W_p . The spin-excited states $|S_i^\alpha\rangle$ introduce two visons associated with the bond along α -direction joint with the i -site. While the spin-dimer excited state $|\mathcal{K}_i^x\rangle$ does not induce any vortex in the vicinity of the impurity tensor, $|\mathcal{K}_i^y\rangle$ and $|\mathcal{K}_i^z\rangle$ harbor four visons.